Turing instability and current-driven self-sustained waves in Dirac fluids

Prayoga Liong,[1, *] Aliaksandr Melnichenka,[2, *] Anton Bukhtatyi,[3] Albert Bilous,[4] and Leonid Levitov[5]

[1]*Department of Physics, Boston University, Boston MA 02215, USA*
[2]*Department of Physics, Berea College, Berea, KY 40404, USA*
[3]*Department of Physics, V. N. Karazin Kharkiv National University, Kharkiv, Ukraine*
[4]*Department of Physics, Taras Shevchenko National University, Kyiv, Ukraine*
[5]*Department of Physics, Massachusetts Institute of Technology, Cambridge MA02139, USA*
(Dated: November 23, 2025)

Viscous films flowing down an incline can form self-sustained running waves, known as Kapitsa roll waves. Here we describe an analogous electron-hydrodynamic instability that produces similar running waves in Dirac materials such as graphene mono- and multilayers. It arises when carrier kinetics near charge neutrality make current dissipation strongly density-dependent. As the flow velocity u exceeds a critical value, the system transitions to a state with coupled spatial and temporal oscillations. Experimentally, the instability should manifest as (i) a nonanalytic behavior characteristic of a second-order transition—an abrupt increase in time-averaged current—and (ii) narrow-band emission at the characteristic "washboard" frequency $f = u/\lambda$, where λ is the modulation wavelength. This behavior parallels the AC and DC transport of sliding charge-density waves, but here it originates from a distinct, intrinsic mechanism unrelated to disorder. Estimates indicate that the emission frequency f, tunable by current, spans a broad range, highlighting Dirac bands as a promising platform for high-frequency electron-fluid dynamics.

Turing instability is a fundamental mechanism of nonequilibrium self-organization [1–3]. Despite the universality of its underlying principles, it has been studied almost exclusively in classical systems. Here, we predict a quantum analogue—a modulational instability in quantum materials driven out of equilibrium by a DC current—and identify the mechanism and conditions under which this collective behavior emerges. The key idea is that an applied current can selectively soften the system at certain wave numbers, making it unstable to periodic modulation. We show that such current-driven Turing instability can occur in quantum dissipative systems such as Dirac and Weyl metals, where electron–hole scattering enhances resistivity and dissipation near charge neutrality (CNP) while keeping them low away from it [10, 11].

The instability mechanism proposed here is reminiscent of the Kapitsa instability in viscous films flowing down an incline, where a steady laminar flow of an open-surface film spontaneously develops periodic modulations [21–26]. The balance between gravity and viscous stress, $-\rho g \sin\theta = \eta\nabla^2 \boldsymbol{v}(\boldsymbol{r})$, where θ is the incline angle, g gravity, and η viscosity, — results in a scaling between flow velocity and film thickness, $u \propto w^2$. As the drag coefficient decreases rapidly with w, regions with slightly larger $w(x)$ will flow faster, thereby amplifying perturbations and giving rise to a self-sustained running wave,

$$w(x) = \bar{w} + \delta w \cos k(x - ut). \tag{1}$$

In fluid films, the wavelength $\lambda = 2\pi/k$ and modulation amplitude are set by the competition between viscous and capillary forces [22]. The emerging wavenumber k coincides with k_*—the wavevector at which the instability growth rate is maximal—mirroring the essence of Turing's pattern-formation mechanism [23].
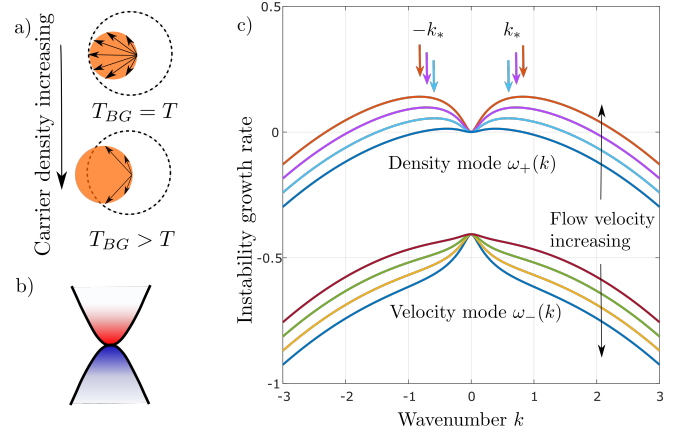

FIG. 1. (a), (b) Examples of current-relaxing kinetics in semiconductors and semimetals in the absence of disorder—the Bloch–Grüneisen crossover in electron–phonon scattering and quasiparticle scattering in a Dirac plasma. In both cases, current dissipation freezes out as carrier concentration grows, a behavior that can drive the Turing–Kapitsa instability. (c) Instability growth rate $\mathrm{Im}\,\omega_\pm(k)$ for the density and velocity modes $\omega_+(k)$ and $\omega_-(k)$, Eq. (18). The density mode, satisfying $\omega_+(0) = 0$ by particle-number conservation, becomes unstable above a critical flow velocity (Eq.(??)); the growth rate $\mathrm{Im}\,\omega_+(k) > 0$ peaks at the wave numbers $\pm k_*$ marked by arrows. The velocity mode remains damped, $\mathrm{Im}\,\omega_-(k) < 0$. Small initial perturbations grow into a periodic modulation with wavelength $\lambda \sim 2\pi/k_*$ propagating downstream; as shown in Fig. 2.

As we will see, an electronic analogue of this instability can cause a steady (DC) electron flow to spontaneously develop self-sustained charge and current oscillations. The correspondence between an atomically thin 2D conductor with carrier density $n(x, y)$ and a classical viscous film with spatially varying thickness $w(x, y)$—measured between the substrate and its free surface—is established
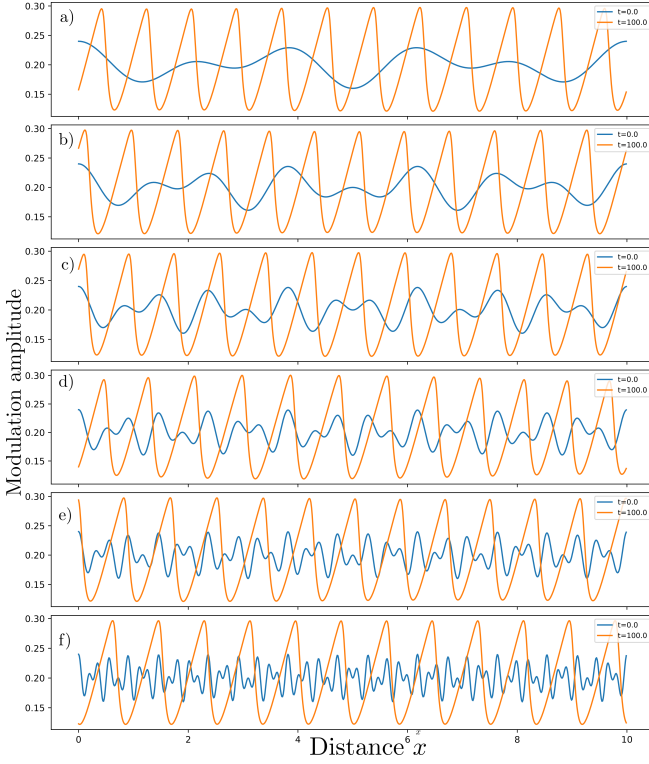
FIG. 2. Wavelength selection at instability. Shown is the long-time modulation (orange) evolved from different initial perturbations (blue): $\delta n(x) = \sum_m a_m \cos k_m x + b_m \sin k_m x$, $\delta p(x) = \sum_m a'_m \cos k_m x + b'_m \sin k_m x$, with $k_m = \frac{2\pi}{L} \times 3, 5, 8, 13, 21, 55$. Regardless of initial conditions, the system converges to the same spatial pattern, with wavelength set by the wavenumber k of maximal growth (marked by arrows in Fig. 1), consistent with Turing's maximum-growth rule.

by identifying $n(x, y)$ with $w(x, y)$. Beyond this "hyperspace mapping" $w(x, y) \to (x, y, n)$, realizing the Turing–Kapitsa instability requires a dissipation mechanism whose rate varies rapidly with n—the electronic analogue of a drag coefficient in viscous films that decreases sharply with increasing film thickness.

There are several effects documented in the literature that can make dissipation drop as carrier concentration grows, see Fig.1 a), b). One is 'intrinsic resistivity' of clean 2D metals with a small Fermi surface due to electron-phonon (e-ph) scattering in the absence of disorder or Umklapp processes. Because e-ph kinetics is quenched at temperatures below the Bloch-Gruneisen temperature $T_{\text{BG}} = 2\hbar s k_F / k_B$, where k_F is Fermi momentum and s is sound velocity, at $T < T_{\text{BG}}$ the e-ph scattering rate is a rapidly decreasing function of carrier concentration, falling off as $n^{-3/2}$ in both graphene monolayers and bilayers [12, 13, 15–20]. Another mechanism is current dissipation due to electron-hole (e-h) scattering at CNP in Dirac bands [4–11]. This effect has a high rate at CNP where Dirac plasma is e-h-balanced, but weakens rapidly upon concentration detuning away
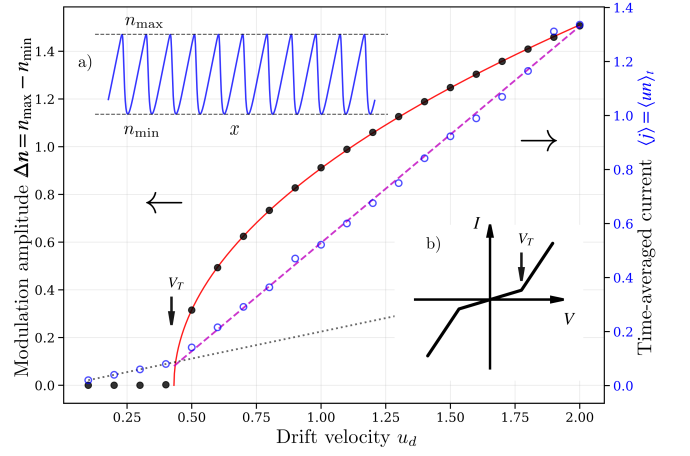

FIG. 3. Electronic Turing–Kapitsa instability driven by current produces self-sustained waves. Plotted are the modulation amplitude and time-averaged current near the instability onset, obtained numerically for a graphene bilayer model (see text). The red line shows the theoretical square-root behavior $\Delta n \propto (u_d - u_d^*)^{1/2}$. The sharp slope change in the current–field dependence marks the instability threshold and the added current from the running waves. Insets (a) and (b) illustrate a typical modulation and the current–field relation.

from CNP. As discussed below, both scattering mechanisms, e-ph and e-h, impact electron dynamics in the same way as width-dependent viscous drag in viscous films, rendering electron flows at densities detuned from CNP unstable once the drift velocity exceeds a critical value and giving rise to running waves propagating downstream.

The self-sustained modulation emerges above the instability threshold in the flow velocity, displaying a continuous second-order phase transition (see Fig. 3). The modulation periodicity λ is governed by the most unstable harmonic $k_* = 2\pi/\lambda$, as expected from the Turing instability criterion. Observable signatures of this collective dynamics resemble those studied for other running wave phenomena, such as sliding charge-density and spin-density waves (CDW and SDW) [27–29]. One is a narrow-band emission at the "washboard" frequency $f = u/\lambda$, where u is the flow velocity tunable by the applied DC current. Another is a characteristic nonlinearity in the current–field dependence at the instability threshold, shown in Fig.3. The increase in the slope of the current vs. u dependence reflects the contribution of running waves to nonlinear conductivity, resembling the Lee-Fukuyama-Rice conductivity of sliding CDW[27–29].

We stress that both the AC emission by running waves at a frequency $f = u/\lambda$ and the DC current nonlinearity are intrinsic effects, present already in a homogeneous system. This is in contrast to CDW sliding, where narrow-band emission and current nonlinearity are governed by the effects due to pinning-depinning by disorder.

To explore the emergence of running waves under Turing-Kapitsa instability driven by a DC current, we

consider a simple but realistic transport model.

A natural framework to analyze collective dynamics of electrons is provided by hydrodynamic equations for particle number and momentum density $n(x,t)$ and $\boldsymbol{p}(x,t)$. Microscopically, these quantities are [spin, valley?]

$$n(x,t) = \sum_{\boldsymbol{p}'} f(\boldsymbol{p}', x, t), \quad \boldsymbol{p}(x,t) = \sum_{\boldsymbol{p}'} \boldsymbol{p}' f(\boldsymbol{p}', x, t), \quad (2)$$

where $f(\boldsymbol{p}, x, t)$ is particle phase-space distribution that evolves in time under the kinetic equation [30, 31]

$$(\partial_t + \boldsymbol{v} \cdot \partial_{\boldsymbol{x}} + \boldsymbol{F} \cdot \partial_{\boldsymbol{p}}) f(\boldsymbol{p}, \xi) = I[f]. \quad (3)$$

Here, $\boldsymbol{v} = \partial_{\boldsymbol{p}} \epsilon(p)$ is the velocity, $\boldsymbol{F} = e\boldsymbol{E}$ the force, and $I[f]$ the collision integral describing electron-electron and electron-hole scattering, and interactions with disorder and phonons; $\xi = (x, t)$ denotes space and time variables.

In what follows, we analyze transport in a parabolic Dirac band of a graphene bilayer. For simplicity, we consider a one-species model representing one component of the bilayer bands—either electron or hole:

$$\epsilon(p) = \frac{\boldsymbol{p}^2}{2m}, \quad m \approx 0.04 m_{\mathrm{e}}, \quad (4)$$

where m_{e} is the free-electron mass. The results below are largely insensitive to the exact form of $\epsilon(p)$ or to microscopic details of how momentum dissipation varies with carrier density. We model this by a dissipation rate that peaks in the region of width $w \sim k_B T$ and decreases with detuning from the CNP[10, 11]:

$$\gamma(n) = \gamma_0 e^{-|n|/w}, \quad w = \frac{2m}{\hbar^2} k_B T + w_0, \quad (5)$$

where the term linear in T describes the CNP width due to intrinsic e-h scattering in pristine graphene, while w_0 accounts for residual CNP broadening from electron–hole puddles that persist down to $T = 0$.

In this model, electron temperature is replaced by an effective time-averaged value, ignoring the electron temperature dynamics. While heating is undoubtedly an important effect, it occurs on times scales considerably longer than those typical for oscillatory electron dynamics. Furthermore, recent experiments[32–34] demonstrate that high currents can be driven through moire graphene at drift velocity reaching the band velocity without strongly overheating the graphene system. This is enabled by efficient cooling due to hBN substrate that allows to drive high currents without damaging graphene system and without broadening the singularities due to Dirac points in graphene bandstructure.

When applied to the particle number and momentum densities, n and p, Eq.(3) gives conservation laws:

$$(\gamma(n) + \partial_t)\boldsymbol{p}(\xi) + \partial_{\boldsymbol{x}} \Pi_0(\xi) = en\left(\boldsymbol{E} - \partial_{\boldsymbol{x}} \Phi(\xi)\right)$$
$$\partial_t n(\xi) + \partial_{\boldsymbol{x}}[n(\xi)\boldsymbol{v}(\xi)] = 0. \quad (6)$$

Here the first equation is the continuum version of the second Newton's law $dp/dt = F$, the second equation is the continuity equation for n. In a parabolic band, momentum density is related to particle current density $\boldsymbol{j} = \sum_{p'} \boldsymbol{v}(p') f(\boldsymbol{p}') \equiv n\boldsymbol{v}$ as $m\boldsymbol{j} = \boldsymbol{p}$.

The quantity Π_0 is the Fermi pressure of a flowing Fermi sea (FS). For Doppler-shifted Fermi distribution $f(\boldsymbol{p}) = \frac{1}{e^{\beta(\epsilon(p) - \boldsymbol{u} \cdot \boldsymbol{p} - \mu)} + 1}$ describing electron gas of density n flowing with the velocity u, Π_0 is a sum of a static contribution and a kinetic energy term

$$\Pi_0 = \sum_{\boldsymbol{p}'} p'_x v_x(\boldsymbol{p}') f(\boldsymbol{p}') = \frac{n^2}{2\nu} + \frac{p^2}{nm}, \quad p = mnu, \quad (7)$$

where $\nu = n/\epsilon_F = gm/2\pi\hbar^2$ is the density of states (g is spin and valley degeneracy). The simple form of the result in Eq.(7), which is a sum of the pressure of a Fermi sea at rest $\Pi_0(n) = \sum_{p'} \epsilon(p') f_{u=0}(p') = n^2/2\nu$ and the Bernoulli pressure p^2/nm due to the flow, is a property of a parabolic band arising from its Galilean symmetry.

The transport equations in Eqs.(6) capture the essential physics underlying the current-driven Turing instability. A more realistic description, however, must explicitly include the interaction and viscous effects incorporated in the hydrodynamic stress density Π.

Below, for conciseness, we use a constant interaction model deferring the discussion of long-range interaction till later. In this case, the last term in (6) takes the form

$$\Phi(\xi) = U_0[n(\xi) - \bar{n}], \quad (8)$$

where constant $\bar{n}$ represents an offset charge on a gate.

It is convenient to combine the terms $\partial_{\boldsymbol{x}}\Pi_0$ and $\partial_{\boldsymbol{x}}\Phi$ in Eq. (6) into a net Fermi pressure term $\partial_{\boldsymbol{x}}\Pi$ that accounts for both electron–electron interactions and the flow, [35]

$$\Pi = \frac{1}{2} U \left(n(\xi)\right)^2 + \frac{(p(\xi))^2}{mn(\xi)}, \quad U = U_0 + \frac{1}{\nu}, \quad (9)$$

where n and p are particle and momentum densities. After these rearrangements, transport equations read

$$(\gamma(n) + \partial_t)\boldsymbol{p}(\xi) + \partial_{\boldsymbol{x}}\Pi(\xi) = en\boldsymbol{E} \quad (10)$$

$$\partial_t n(\xi) + \frac{1}{m}\partial_{\boldsymbol{x}}\boldsymbol{p}(\xi) = 0, \quad (11)$$

where in the continuity equation we replaced nv with p/m. A steady uniform current-carrying state obeys

$$\gamma\boldsymbol{p} = en\boldsymbol{E}, \quad (12)$$

yielding a standard result for the flow velocity, $\gamma u = \frac{e}{m}E$. Next, we show that Eqs. (10) and (11) predict instability of a current-carrying state.

Perturbing the steady state as $n = \bar{n} + \delta n$, $p = \bar{p} + \delta p$, we examine the conditions under which the transport equations develop an instability. It will become clear below that it is beneficial to regularize the dynamics at

large wavenumbers by introducing diffusion terms in the p and n equations. This can be done by replacing

$$\partial_t p \to (\partial_t - D_p \partial_x^2)p, \quad \partial_t n \to (\partial_t - D_n \partial_x^2)n \quad (13)$$

in Eqs.(10) and (11). This change does not affect the behavior of the linearized problem at long wavelengths, provided D_n and D_p are small, however it makes the dynamics well behaved at short wavelengths, allowing to perform numerical simulations and explore the behavior at long times where the nonlinear behavior triggered by Turing instability emerges. [Write about numerical procedure.]

Linearizing Eqs.(10) and (11). in n and p, gives

$$(\gamma_n \bar{p} - eE)\,\delta n + \Pi_n \partial_x \delta n + \gamma \delta p + (\partial_t - D_p \partial_x^2)\delta p$$
$$+ \Pi_p \partial_x \delta p = 0, \quad (\partial_t - D_n \partial_x^2)\delta n + \frac{1}{m}\partial_x \delta p = 0, \quad (14)$$

where the quantities with subscripts n and p denote partial derivatives: $\gamma_n = \partial\gamma/\partial n$, $\Pi_n = \partial\Pi/\partial n$ and $\Pi_p = \partial\Pi/\partial p$. For harmonic perturbations $\delta n(\xi) = \delta n_{\omega,k} e^{ikx - i\omega t}$, $\delta p(\xi) = \delta p_{\omega,k} e^{ikx - i\omega t}$ this problem yields a pair of coupled linear equations

$$(\Lambda + ik\Pi_n)\delta n_{\omega,k} + (\gamma - i\omega + D_p k^2 + ik\Pi_p)\delta p_{\omega,k} = 0$$
$$(-i\omega + D_n k^2)\delta n_{\omega,k} + i\frac{k}{m}\delta p_{\omega,k} = 0 \quad (15)$$

where we used a shorthand notation $\Lambda = \left(\frac{\partial\gamma}{\partial n} - \frac{\gamma}{n}\right)p$. Instability occurs when the linearized problem admits a complex-frequency solution growing with time,

$$\delta n_k(t),\, \delta p_k(t) \sim e^{-i\omega t}, \quad \mathrm{Im}\,\omega_+(k) > 0. \quad (16)$$

The characteristic equation for this problem, in matrix form, reads

$$\begin{pmatrix} \Lambda + ik\Pi_n & \gamma - i\omega + D_p k^2 + ik\Pi_p \\ -i\omega + D_n k^2 & i\frac{k}{m} \end{pmatrix} \begin{pmatrix} \delta n_{\omega,k} \\ \delta p_{\omega,k} \end{pmatrix} = 0. \quad (17)$$

This yields two normal modes with frequencies

$$\omega_\pm(k) = \frac{-i\tilde{\gamma} + k\Pi_p \pm i\sqrt{\Delta}}{2} - iD_n k^2, \quad (18)$$

where $\tilde{\gamma} = \gamma + (D_p - D_n)k^2$ and

$$\Delta = (\tilde{\gamma} + ik\Pi_p)^2 + \frac{4ik}{m}\Lambda - \frac{4k^2}{m}\Pi_n. \quad (19)$$

This general result is applicable to systems with both low and high dissipation, and both in the absence and in the presence of the flow. At $k = 0$ the frequency ω_+ vanishes, whereas the frequency ω_- takes a negative-imaginary value, corresponding to the conserved density and relaxing velocity modes, respectively.

Before analyzing amplification and instability in the strongly dissipative regime $\gamma \gg \omega$—the main focus of this

work—it is useful to verify that, in the weak-dissipation limit, our results reproduce the known plasma mode dispersions, both with and without steady background flow. Setting γ, Λ, D_n and D_p to zero gives

$$\omega_\pm(k) = \frac{1}{2}k\Pi_p \pm \sqrt{\frac{1}{4}k^2\Pi_p^2 + \frac{1}{m}k^2\Pi_n}, \quad (20)$$

where we moved i under the square root. Focusing on a parabolic band and plugging $\Pi_p = 2p/nm$ and $\Pi_n = Un - p^2/n^2 m$ [with U the sum of the ee interaction and Fermi sea pressure contributions, as given in Eq.(9)] the p dependence under the square root cancels, giving

$$\omega_\pm(k) = ku \pm ku_0, \quad u_0 = \sqrt{Un/m}. \quad (21)$$

Here u_0 is plasmon velocity at density n and u is the flow velocity, $p = mnu$. This gives the Doppler-shifted undamped plasma dispersion $(\omega - uk)^2 = k^2 u_0^2$, as expected from Galilean symmetry for a parabolic band.

MAXIMALLY UNSTABLE WAVELENGTH AND INSTABILITY THRESHOLD

Next, we proceed with the analysis of dissipative transport. It is instructive to focus on the strongly dissipative regime, where the momentum relaxation rate γ greatly exceeds scales such as ωp and $k\Pi$. For the parabolic band model the general expression for mode frequencies given in Eqs. (18) and (19) simplify considerably. Substituting the derivatives Π_n and Π_p in Eq. (19) yields

$$\Delta = \gamma^2 + ik\frac{4p}{m}\frac{d\gamma}{dn} - k^2\frac{4Un}{m} \quad (22)$$

An analytic estimate of the most unstable wavelength k_* can be obtained by examining the instability growth rate $\zeta(k) = \mathrm{Im}\,\omega_+(k)$ vs. k in the limits of small and large k, and matching the two asymptotic behaviors in the intermediate ("borderline") region. For clarity, we focus on the case of small diffusion coefficients D_n and D_p, setting $D_n = D_p = 0$. In the large-k limit ($k \gg k_*$), the growth rate approaches a k-independent value:

$$\zeta(k)_{k \gg k_*} = -\frac{1}{2}\gamma + \frac{s}{2u_0}\frac{pd\gamma}{mdn}, \quad s = \mathrm{sgn}\left(p\frac{d\gamma}{dn}\right). \quad (23)$$

This predicts the instability threshold at

$$p\frac{d\gamma}{dn} = s\gamma m u_0 \quad (24)$$

with an unstable phase for $p\frac{d\gamma}{dn}s > \gamma m u_0$ and a stable phase for $p\frac{d\gamma}{dn} < \gamma m u_0$. Namely, the instability occurs when the flow velocity $u = p/mn$ exceeds the critical value, $u > u_c$, where

$$u_c = \frac{u_0}{R}, \quad R = \left|\frac{d\log\gamma}{d\log n}\right| \quad (25)$$

Estimate velocity u_c. If R is order-one, the flow velocity at which instability occurs is comparable to the plasmonic velocity $u_0 = \sqrt{Un/m}$. However, we stress that, since the dissipative regime of interest typically occurs near CNP, the density n values can be much smaller than those at which weakly damped plasmons are observed. State-of-the-art measurements [REF Basov] report plasmon velocities u_p for carrier concentration $n = ...$, whereas the BG suppression of el-ph kinetics is observed at $n \sim ...$, yielding the values $u_0 = ...$ The exact values $\gamma(n)$ and R will depend on the mechanism that makes dissipation a function of carrier density.

Next, to complete the estimate of the most unstable wavelength we consider small k, where Taylor expansion of $\zeta(k)$ to leading order in k gives

$$\zeta(k \ll k_*) = k^2 \left[\frac{p^2 \left(\frac{d\gamma}{dn} \right)^2}{m^2 \gamma^3} - \frac{u_0^2}{\gamma} \right] + O(k^4) \qquad (26)$$

For $k \approx k_*$, these values must agree with those in Eq.(23). Writing this condition as

$$k_*^2 \left[\frac{p^2 \left(\frac{d\gamma}{dn} \right)^2}{m^2 \gamma^3} - \frac{u_0^2}{\gamma} \right] = \frac{p \frac{d\gamma}{dn}}{2mu_0} - \frac{1}{2}\gamma \qquad (27)$$

and noting that both the left- and the right-hand side vanish at the transition but remain nonzero away from transition, we obtain

$$k_*^2 \approx \frac{1}{4} \frac{\gamma^2}{u_0^2}. \qquad (28)$$

Notably, the maximally unstable wavelength, $\lambda_* = 2\pi/k_*$, remains finite at the transition. This behavior is consistent with our simulation results and mirrors the finite modulation wavelength observed in the hydrodynamic Kapitsa instability[23, 24].

Finite D_n and D_p may shift the instability threshold and λ_*. However, at small D_n and D_p this effect is expected to be small.

[Do we agree with these estimates? If so, let's estimate numerical values for λ_* and u_c]

To compare the critical velocity to band velocity v_F and plasmonic velocity, we consider momentum dissipation that peaks at small n and drops to zero at larger n, Eq.(5), as expected to be the case at band crossing in graphene and similar bandstructures [4–11]. In this case, ohmic resistivity depends on density as $\rho(n) \sim \gamma(n)/n$, showing a peak at $n = 0$ and rapidly decreasing as n grows, which mimics the behavior in Dirac bands. Eq.(25) then predicts instability at

$$u_c = \sqrt{\frac{U}{mn}} w. \qquad (29)$$

Notably, if dissipation changes rapidly with n, as it happens in graphene near the CNP, the critical velocity u_c is pushed to lower values, making the instability more readily accessible. Therefore, in the dissipative regime the critical velocity can be much smaller than the band velocity and the plasma excitation velocity.

Add estimates of critical velocity in the units of v_F, discuss the weak dependence on k and w. Behavior at criticality. Nonlinear effects. The sawtooth waveform and Turing wavelength selection problem.

Questions: Classical vs. quantum? Electron regime—dissipative and viscous–leads to high-frequency dynamics (THz range). What is the frequency, what controls it?

Discussion with Leo R: Let's point to specific places in the instability analysis where the Kapitsa mechanism plays out. How sensitive is the instability to the details of the $\gamma(n)$ dependence? Can it be mapped directly to the original Kapitsa's analysis of Kapitsa instability problem, in which the dynamics of a thin layer of a 3D fluid is reduced to a 2D problem similar to ours by integration over layer cross-section? Is $\gamma \sim 1/n^2$ in this case?

Connect to the treatment in the paper on $R = 0$ and negative dV/dI in a B field (Fisher, Balents, Radzikhovsky).

Comment on nonlinear I-V dependence observed in various experiments (Koppens, Morpurgo, Lau, Dean)

Comment on high current values and (potentially) exceptionally high narrow-band emission frequency

NUMERICAL PROCEDURE

In this section, we describe the numerical procedure used to solve the hydrodynamic transport equations for the main variables: the particle density $n(x,t)$ and the momentum density $p(x,t) = mnu$. These equations take the form:

$$\partial_t n = -\partial_x \frac{p}{m} + D_n \partial_x^2 n, \qquad (30)$$

$$\partial_t p = -\gamma(n)p - \partial_x \left(\frac{U}{2}n^2 + \frac{p^2}{mn} \right) + enE + D_p \partial_x^2 p,$$

where E is a spatially uniform driving field, U is electron-electron interaction, D_p and D_n are diffusivity parameters introduced to regularize the dynamics (and taken to be small and positive). In simulations, we nondimensionalize the problem by setting $m = e = 1$ and, in this paper, work with $n(x)$ and $p(x)$ defined on a finite interval $0 < x < L$, obeying Eqs.(30) and (??) with periodic boundary conditions, $n_{x=0} = n_{x=L}$, $p_{x=0} = p_{x=L}$.

The results shown in Fig. 2 and Fig. 3 have been produced by the numerical procedure summarized below. We discretize space, and integrate in time adaptively. Spatial derivatives are computed in Fourier space (e.g., [37, 40, 41]) for high accuracy on periodic domains, and time integration uses a stiff Backward Differentiation

Formula (BDF) method [39]. The solver automatically adjusts the time step to satisfy the prescribed error tolerances. Throughout, divisions by n are regularized with $n_{\min} = 10^{-7}$ in denominators; this has no discernible effect on converged solutions but avoids numerical singularities.

The functions $n(x)$ and $p(x)$ were represented as discrete Fourier series evaluated on an equispaced grid of N_x points. Each right-hand side evaluation scales as $\mathcal{O}(N_x \log N_x)$ due to FFTs. Because accurate wave resolution is required, we choose around 30–50 grid points per dominant wavelength to capture active scales without over-resolving the grid.

For improved numerical accuracy, we compute the spatial derivatives in Eqs. (30) in Fourier space. For a given target accuracy, this allows us to use fewer grid points than low-order finite differences, which can reduce the overall computational cost. Specifically, we obtain the first and second derivatives by multiplying the field by ik and $-k^2$, respectively, and then transforming back to physical space. Nonlinear products (such as the pressure and damping contributions) are formed pointwise in x space and returned to k space by Fast Fourier Transform (FFT).

To control aliasing from these nonlinearities we apply the Orszag 2/3 truncation rule: after each right-hand-side evaluation we zero all modes with $|k| > (2/3)k_{\max}$, where $k_{\max} = \pi/\Delta x$ and $\Delta x = L/N_x$ [36].

On a finite grid, quadratic products generate Fourier interactions beyond the Nyquist wavenumber [37]. These spurious components appear at incorrect lower frequencies or wavelengths unless they are filtered out. Keeping only the lowest two–thirds of modes guarantees [36] that every quadratic interaction of retained modes either stays within the allowed range or falls completely outside it, where it is removed.

We use the method of lines (MOL), discretizing the spatial coordinate to convert the PDEs into a system of ordinary differential equations (ODEs) in time. The system is integrated in time using a *BDF* integrator implemented through the *solve_ivp* function from the SciPy library [38]. This method automatically adjusts how many past time levels it uses during the run, allowing it to maintain accuracy and stability for stiff problems. The solver uses the relative and absolute tolerances rtol $= 10^{-4}$ and atol $= 10^{-7}$. These tolerance values were determined through numerical experiments as optimal: reducing them further increases runtime, while loosening them may introduce numerical artifacts. Therefore, when accuracy concerns arise, we refine the spatial discretization N_x and adjust the tolerance parameters accordingly.

The BDF integrator automatically adjusts the time step (and the method order) using a local error estimate so that the weighted local truncation error remains within the specified tolerances. The spatial discretization is fixed once a run begins: both the number of grid points N_x and the domain length L remain constant for the duration of the simulation.

The domain length L is chosen so that the discrete wavenumber set $\{k_m = 2\pi m/L\}$ contains the most unstable linear wavenumber k^*. Once chosen, L and N_x are kept fixed during the simulation.. We first pick an integer $1 < M < 15$ representing the intended number of wavelengths in the box and set

$$L = \frac{2\pi M}{k^*} \tag{31}$$

so that k^* coincides exactly with the grid mode k_M. We then select N_x large enough that the de-aliased band retains not only k^* but also its first few harmonics; in practice we enforce $M \leq N_x/9$. The box size and initial conditions are decided before the run and are not altered during the simulation.

Simulations start from a spatially uniform drifting state, $n(x,0) = \bar{n}$ and $p(x,0) = m\bar{n}u_d$. To seed pattern formation we add a small, deterministic superposition of sine and cosine modes,

$$n(x,0) = \bar{n} + \sum_{j \in \mathcal{S}} (a_j \cos k_j x + b_j \sin k_j x), \tag{32}$$

$$p(x,0) = m\bar{n}u_d + \sum_{j \in \mathcal{S}} (a'_j \cos k_j x + b'_j \sin k_j x). \tag{33}$$

where $k = \frac{2\pi j}{L}$ with j spanning a finite set of low integers (for example $\{3, 5, 8, 13, 21\}$) and moderate values of the coefficients a_j, a'_j, etc., were chosen, typically $a_j, b_j \lesssim 0.2\bar{n}$ and $a'_j, b'_j \lesssim 0.2m\bar{n}u_d$. As illustrated in Fig. 2, the system converges to near-identical spatial patterns regardless of the initial conditions.

The density-dependent damping is implemented as Eq. 5. The pressure entering the momentum balance is Eq. 9. The electric field E is taken to be uniform in space.

---

[*] Equal contributions

[1] A. M. Turing, The Chemical Basis of Morphogenesis, Philos. Trans. R. Soc. Lond. B **237**, 37 (1952).

[2] J. D. Murray, Mathematical Biology, 3rd ed. (Springer, 2002).

[3] I. Prigogine and G. Nicolis, Self-Organization in Nonequilibrium Systems (Wiley, 1977).

[4] L. Fritz, J. Schmalian, M. Müller and S. Sachdev, Quantum-critical transport in clean graphene, Phys. Rev. B **78**, 085416 (2008).

[5] M. Müller, J. Schmalian and L. Fritz, "Graphene: a nearly perfect fluid" Phys. Rev. Lett. **103**, 025301 (2009).

[6] A. B. Kashuba, "Conductivity of defectless graphene," Phys. Rev. B **78**, 085415 (2008).

[7] P. Gallagher et al., Quantum-critical conductivity of the Dirac fluid in graphene, Science 364, 158-162 (2019).

[8] M. J. H. Ku et al., Imaging viscous flow of the Dirac fluid in graphene Nature 583 (7817), 537–541 (2020).

[9] A. Lucas, J. Crossno, K. C. Fong, P. Kim and S. Sachdev, Transport in inhomogeneous quantum critical fluids and in the Dirac fluid in graphene, Phys. Rev. B 93, 075426 (2016).

[10] Y. Nam, D.-K. Ki, D. Soler-Delgado and A. F. Morpurgo, Electron-hole collision limited transport in charge-neutral bilayer graphene, Nature Physics 13, 1207-1214 (2017).

[11] A. Lucas and K. C. Fong, Hydrodynamics of electrons in graphene, J. Phys.: Condens. Matter 30 053001 (2018).

[12] H. L. Störmer, L. N. Pfeiffer, K. W. Baldwin, and K. W. West, "Observation of a Bloch–Grüneisen regime in two-dimensional electron transport," Phys. Rev. B 41, 1278–1281 (1990).

[13] D. K. Efetov and P. Kim, "Controlling Electron-Phonon Interactions in Graphene at Ultrahigh Carrier Densities," Phys. Rev. Lett. 105, 256805 (2010).

[14] M. S. Fuhrer, Textbook physics from a cutting-edge material, Physics 3, 106 (2010).

[15] E. H. Hwang and S. Das Sarma "Acoustic phonon scattering limited carrier mobility in two-dimensional extrinsic graphene," Phys. Rev. B 77, 115449 (2008).

[16] C.-H. Park, N. Bonini, M. Calandra, and F. Mauri, "Electron–Phonon Interactions and the Intrinsic Electrical Resistivity of Graphene," Nano Letters 14, 1113–1119 (2014).

[17] K. Kaasbjerg, K. S. Thygesen, and K. W. Jacobsen, "Unraveling the acoustic electron–phonon interaction in graphene," Phys. Rev. B 85, 165440 (2012).

[18] J. K. Viljas and T. T. Heikkilä, "Electron–phonon heat transfer in monolayer and bilayer graphene," Phys. Rev. B 81, 245404 (2010).

[19] O. E. Raichev, A. T. Hatke, M. A. Zudov and J. L. Reno, "Bloch-Grüneisen nonlinearity of electron transport in GaAs/AlGaAs heterostructures," Phys. Rev. B 96, 081407(R) (2017).

[20] R. Bistritzer and A. H. MacDonald, "Electronic cooling in graphene," Phys. Rev. Lett. (arXiv:0901.4159) (2009).

[21] R. V. Craster and O. K. Matar, Dynamics and stability of thin liquid films, Rev. Mod. Phys. 81, 1131 (2009).

[22] P. L. Kapitza, Wave formation on the surface of a viscous fluid flowing down an inclined plane, Zh. Eksp. Teor. Fiz. 18, 3 (1948).

[23] A. F. Andreev, Stability of the laminar flow in thin liquid layers, J. Exp. Theor. Phys. 45, 755-759 (1964) [Engl. transl.: JETP, Vol. 18, No. 2, p. 519 (1964)].

[24] N. J. Balmforth and S. Mandre, Dynamics of roll waves, J. Fluid Mech. 514, 1-33 (2004)

[25] B. P. Chimetta, M. Z. Hossain, E. de Moraes Franklin, Numerical solution for Kapitza waves on a thin liquid film, arXiv:1807.05613

[26] Video of the Kapitza effect: melting snow creates a downhill stream that turns unstable and forms roll waves, as described by thin-film hydrodynamics[22–25].

[27] P. A. Lee and H. Fukuyama, Phys. Rev. B 17, 542 (1972); H. Fukuyama and P. A. Lee, Phys. Rev. B 17, 535 (1978).

[28] P. A. Lee and T. M. Rice, Phys. Rev. B 19, 3970 (1979).

[29] G. Grüner, The dynamics of charge-density waves, Rev. Mod. Phys. 60, 1129 (1988).

[30] E. M. Lifshitz and L. P. Pitaevsky, "Physical Kinetics" (Butterworth-Heinemann 1981).

[31] D. Tong, "Kinetic Theory," University of Cambridge Graduate Course 2012.

[32] A. I. Berdyugin, N. Xin, H. Gao, S. Slizovskiy, Z. Dong, S. Bhattacharjee, P. Kumaravadivel, S. Xu, L. A. Ponomarenko, M. Holwill, D. A. Bandurin, M. Kim, Y. Cao, M. T. Greenaway, K. S. Novoselov, I. V. Grigorieva, K. Watanabe, T. Taniguchi, V. I. Falko, L. S. Levitov, R. Krishna Kumar, and A. K. Geim, Out-of-equilibrium criticalities in graphene superlattices, Science, 375, 430-433 (2022).

[33] K. Nowakowski and H. Agarwal and S. Slizovskiy and R. Smeyers and X. Wang and Z. Zheng and J. Barrier and D. Barcons Ruiz and G. Li and R. Bertini and M. Ceccanti and I. Torre and B. Jorissen and A. Reserbat-Plantey and K. Watanabe and T. Taniguchi and L. Covaci and M. V. Milošević and V. Fal'ko and P. Jarillo-Herrero and R. K. Kumar and F. H. L. Koppens, Single-photon detection enabled by negative differential conductivity in moiré superlattices, Science, 389 (6760), 644-649 (2025).

[34] J. Geurs, T. A. Webb, Y. Guo, I. Keren, J. H. Farrell, J. Xu, K. Watanabe, T. Taniguchi, D. N. Basov, J. Hone, A. Lucas, A. Pasupathy, C. R. Dean, Supersonic flow and hydraulic jump in an electronic de Laval nozzle, arxiv.org/abs/2509.16321

[35] This is achieved using the identity

$$n(x)\partial_x \Phi(x) = n(x)\partial_x U_0(n(x) - \bar{n}) = \partial_x \frac{U_0}{2} n^2(x)$$

where density offset parameter $\bar{n}$ originates from Eq. (8) where it was introduced to maintain charge neutrality of the unperturbed equilibrium state. As a quick check on above result and Eq. (8), take a system with no electric field or current, perturbed by a static, position-dependent background $\bar{n}(x)$. The above relation predicts the response of the form $n(x) = \frac{U_0}{U}\bar{n}(x)$, in agreement with the Thomas–Fermi screening picture. As expected, for a system at constant density, $\bar{n}$ drops out from equations of motion, reflecting that only the electrons are moving under electric field, whereas the background charges contributing to $\bar{n}$ remain stationary.

[36] S. A. Orszag,"Elimination of aliasing in finite-difference schemes by filtering high-wavenumber components," Journal of the Atmospheric Sciences 28, 1074-1074 (1971).

[37] C. Canuto, M. Y. Hussaini, A. Quarteroni, and T. A. Zang, "Spectral Methods in Fluid Dynamics" (Springer, Berlin, Heidelberg, 1988).

[38] P. Virtanen, R. Gommers, T. E. Oliphant, M. Haberland, T. Reddy, D. Cournapeau, E. Burovski, P. Peterson, W. Weckesser, J. Bright, S. J. van der Walt, M. Brett, J. Wilson, K. J. Millman, N. Mayorov, A. R. J. Nelson, E. Jones, R. Kern, E. Larson, C. J. Carey, I. Polat, Y. Feng, E. W. Moore, J. VanderPlas, D. Laxalde, J. Perktold, R. Cimrman, I. Henriksen, E. A. Quintero, C. R. Harris, A. M. Archibald, A. H. Ribeiro, F. Pedregosa, P. van Mulbregt, and the SciPy 1.0 Contributors, "SciPy 1.0: Fundamental Algorithms for Scientific Computing in Python", Nature Methods 17, 261-272 (2020).

[39] E. Hairer and G. Wanner, "Solving Ordinary Differential Equations II: Stiff and Differential–Algebraic Problems", 2nd ed. (Springer, Berlin, Heidelberg, 1996).

[40] J. P. Boyd, "Chebyshev and Fourier Spectral Methods", 2nd ed. (Dover Publications, Mineola, NY, 2001).

[41] L. N. Trefethen, "Spectral Methods in MATLAB" (Society for Industrial and Applied Mathematics, Philadelphia, PA, 2000).

ELECTRON-ELECTRON SCATTERING AND CURRENT RELAXATION IN A 2D PARABOLIC SEMIMETAL

As is well known, momentum-conserving electron–electron scattering in semimetals does *not* conserve current: a collision transferring carriers in different bands reverses its current contribution even if overall momentum is conserved. Here we consider carrier collisions in Dirac plasma in a two-band semimetal with parabolic band dispersion

$$\varepsilon_\pm(\mathbf{k}) = \pm\frac{k^2}{2m^*}, \qquad \mathbf{v}_\pm(\mathbf{k}) = \nabla_\mathbf{k}\varepsilon_\pm = \pm\frac{\mathbf{k}}{m^*},$$

representing the conduction $(+)$ and valence $(-)$ bands.

At charge neutrality $(\mu = 0)$, states in the conduction and valence bands with the same momentum $\mathbf{k}$ have *opposite* velocities. As a result, momentum-conserving electron–electron (e–e) collisions that transfer particles between the two bands lead to efficient current relaxation even though total momentum is conserved.

Current-relaxing processes arise because for a generic e–e collision $\mathbf{k}_1, \mathbf{k}_2 \to \mathbf{k}'_1, \mathbf{k}'_2$, momentum is conserved but current is not. Indeed, a generic interband scattering process involving electrons and holes in the conduction and valence bands, respectively, yields a nonzero change in current:

$$\Delta\mathbf{J} = e\big(\mathbf{v}_{s'_1}(\mathbf{k}'_1) + \mathbf{v}_{s'_2}(\mathbf{k}'_2) - \mathbf{v}_{s_1}(\mathbf{k}_1) - \mathbf{v}_{s_2}(\mathbf{k}_2)\big),$$

because $\mathbf{v}_+(\mathbf{k}) = -\mathbf{v}_-(\mathbf{k})$. Thus any process that reshuffles occupation between bands with the *same momentum* relaxes current.

This mechanism is always present in a two-band semimetal and is largest near charge neutrality, where thermally excited electrons and holes coexist.

Quantitatively, this effect and its dependence on doping can be understood by considering the density of states and thermal hole density. For a 2D parabolic semimetal (e.g. bilayer graphene) the density of states is constant:

$$\rho(\varepsilon) = \rho_0 = \frac{m^*}{\pi}.$$

When the chemical potential lies in the conduction band $(\mu > 0)$, current-relaxing interband scattering requires a thermally excited *hole* in the valence band. The density of available valence-band holes is

$$n_h(\mu,T) = \rho_0 \int_0^\infty d\varepsilon\, \frac{1}{1 + e^{(\varepsilon+\mu)/T}},$$

where, for conciseness, we suppress the Boltzmann constant. For $\mu \gg T$ one finds

$$n_h(\mu,T) \approx \rho_0\, T\, e^{-\mu/T}.$$

Thus, for a 2D parabolic semimetal,

$$\boxed{n_h(\mu,T) \propto T\, e^{-\mu/T}}$$

and this single scale controls the strength of current-relaxing e–e processes.

The current-relaxation rate from momentum-conserving e–e collisions is proportional to the availability of interband scattering partners. Thus,

$$\boxed{\frac{1}{\tau_J(\mu,T)} \;\propto\; n_h(\mu,T) \;\propto\; T\, e^{-\mu/T}}$$

for a 2D parabolic semimetal.

At charge neutrality $(\mu = 0)$,

$$\frac{1}{\tau_J} \sim T.$$

Away from neutrality $(\mu \gg T)$,

$$\frac{1}{\tau_J} \sim T\, e^{-\mu/T},$$

showing rapid suppression of this dissipation mechanism with doping.

To put things in perspective, we present a comparison with 3D parabolic semimetals. In a 3D parabolic semimetal with

$$\rho(\varepsilon) \propto \sqrt{\varepsilon}.$$

In this case, similar estimates predict

$$n_h(\mu,T) \sim T^{3/2} e^{-\mu/T}, \qquad \frac{1}{\tau_J} \propto T^{3/2} e^{-\mu/T}.$$

Thus the *mechanism* is dimension-independent, but the *power of T* depends on the DOS.

In summary, for parabolic two-band semimetals:

$$\boxed{\frac{1}{\tau_J(\mu,T)} \propto \begin{cases} T\, e^{-|\mu|/T}, & \text{2D (bilayer graphene)}, \\[6pt] T^{3/2}\, e^{-|\mu|/T}, & \text{3D parabolic semimetal.} \end{cases}}$$

In bilayer graphene the density of states is constant, so the only suppression away from neutrality comes from the Fermi factor $e^{-|\mu|/T}$, leading to a simple, exponential weakening of current-relaxing e–e scattering with doping.

In summary,

- At charge neutrality $(\mu = 0)$: interband particle–hole excitations are abundant; $1/\tau_J \sim T$ with an order-one prefactor and current relaxation is strong.

- At finite doping ($|\mu| \gg T$): valence-band population is exponentially suppressed; $1/\tau_J$ decreases as $\exp(-|\mu|/T)$.

- Compared to Dirac semimetals where $n_h \propto T^2 \exp(-|\mu|/T)$ but the DOS is linear, the parabolic DOS enhances scattering at neutrality but produces the same exponential suppression at finite doping.

References

1. L. Fritz, J. Schmalian, M. Müller, S. Sachdev, *Quantum critical transport in clean graphene*, Phys. Rev. B **78**, 085416 (2008).

2. M. Müller, L. Fritz, S. Sachdev, *Quantum-critical relativistic magnetotransport in graphene*, Phys. Rev. B **78**, 115406 (2008).

3. A. Lucas, K. C. Fong, *Hydrodynamics of electrons in graphene*, J. Phys. Cond. Matt. **30**, 053001 (2018).

4. B. N. Narozhny, I. V. Gornyi, *Electron hydrodynamics in graphene*, Ann. Phys. **529**, 1700043 (2017).

5. Y. Nam, D. K. Efetov et al., *Electron–electron scattering in bilayer graphene*, Science **362**, 1057 (2018).

6. L. Levitov and G. Falkovich, "Electron viscosity, current vortices and negative nonlocal resistance in graphene," *Nature Phys.* **12**, 672 (2016).

7. B. N. Narozhny and M. Schütt, "Hydrodynamic approach to electronic transport in graphene," *Rev. Mod. Phys.* (Colloquium) **96**, 011003 (2024).

8. T. Scaffidi, "Hydrodynamic transport in interacting Fermi liquids," *Phys. Rev. X* **7**, 041048 (2017).

9. P. Ledwith, H. Guo, and L. Levitov, "Angular superdiffusion and momentum space dynamics in 2D electron liquids," *Ann. Phys.* **411**, 167913 (2019).